First-principles thermodynamic modeling of lanthanum chromate perovskites

P. Dalach,[1] D. E. Ellis,[1,*] and A. van de Walle[2]

[1]*Department of Physics and Astronomy, Northwestern University, Evanston, Illinois 60208, USA*

[2]*Department of Engineering and Applied Science Division, California Institute of Technology, Pasadena, California 91125, USA*

(Received 16 May 2011; revised manuscript received 15 November 2011; published 17 January 2012)

Tendencies toward local atomic ordering in $(A,A')(B,B')O_{3-\delta}$ mixed composition perovskites are modeled to explore their influence on thermodynamic, transport, and electronic properties. In particular, dopants and defects within lanthanum chromate perovskites are studied under various simulated redox environments. $(La_{1-x},Sr_x)(Cr_{1-y},Fe_y)O_{3-\delta}$ (LSCF) and $(La_{1-x},Sr_x)(Cr_{1-y},Ru_y)O_{3-\delta}$ (LSCR) are modeled using a cluster expansion statistical thermodynamics method built upon a density functional theory database of structural energies. The cluster expansions are utilized in lattice Monte Carlo simulations to compute the ordering of Sr and Fe(Ru) dopant and oxygen vacancies (Vac). Reduction processes are modeled via the introduction of oxygen vacancies, effectively forcing excess electronic charge onto remaining atoms. LSCR shows increasingly extended Ru-Vac associates and short-range Ru-Ru and Ru-Vac interactions upon reduction; LSCF shows long-range Fe-Fe and Fe-Vac interaction ordering, inhibiting mobility. First principles density functional calculations suggest that Ru-Vac associates significantly decrease the activation energy of Ru-Cr swaps in reduced LSCR. These results are discussed in view of experimentally observed extrusion of metallic Ru from LSCR nanoparticles under reducing conditions at elevated temperature.

DOI: 10.1103/PhysRevB.85.014108 PACS number(s): 61.72.Bb, 61.72.J−, 66.10.Ed

I. INTRODUCTION

Solid oxide fuel cells (SOFCs) are a means to efficiently generate clean electricity from domestic fuel sources, and have been in a constant state of development since 1937.[1] Improving the material components of SOFCs would allow fuel cells to be economically competitive with other means of commercially available power production.[2] Understanding the electronic structural properties and the resulting atomistic properties of SOFC components is central to rapid materials development. In a previous work,[3] an energy cluster expansion was developed for yttria stabilized zirconia (YSZ), the prototypical SOFC electrolyte material, to help understand the effects of atomic ordering of dopant and defects on oxygen ion conductivity.

LSCF $(La_{1-x},Sr_x)(Cr_{1-y},Fe_y)O_{3-\delta}$ and LSCR[4] and $(La_{1-x},Sr_x)(Cr_{1-y},Ru_y)O_{3-\delta}$ are newer materials under evaluation for SOFC electrode applications. As mixed ionic and electronic conductors (MIECs), LSCF and LSCR are potentially ideal electrode materials whose stability, especially at the reducing anode-electrolyte interface, and conductivity properties can be tuned by varying dopant concentrations.[5] Further, LSCR has been shown to precipitate electro-catalytic metallic Ru onto SOFC nanoparticle anode surfaces when exposed to hydrogen fuel at elevated temperature,[6] leading to improved cell performance.[7]

The atomic ordering properties of LSCF and LSCR have not, as of yet, been thoroughly surveyed. Further, simultaneous exploration of both LSCF and LSCR together provide contrast helpful in linking experimentally known dynamic properties to their related and as yet unexplored structural properties, such as diffusion to redox-dependent atomic ordering. This study uses a theoretical approach in which *ab initio* methods are used to construct a statistical thermodynamics model to ascertain characteristic atomic ordering in our studied systems. *Ab initio* techniques will then be reapplied to the structurally resolved systems, focused particularly on further illuminating the mechanism for the reversible precipitation of metallic Ru on the surface of reduced LSCR.

II. METHODOLOGY

In the following sections, procedures are described by which limited sets of first-principles data [density functional theory (DFT) derived, in the present case] are used to determine topological cluster expansions (CE) of concentration- and configuration-dependent properties such as energy and magnetization. Lattice Monte Carlo (LMC) techniques are then used to rapidly sample a wide range of structures at finite temperature, providing a statistical basis for describing thermodynamic and transport properties across a wide phase field. The scheme DFT $=>$ CE $=>$ LMC is shown to be robust and sufficiently rapid to permit analysis of atomic ordering and its probable effects upon dynamical properties like ionic diffusion in complex fuel cell materials.

A. Density functional theory

The structural energy libraries needed for CE construction for LSCR and LSCF were initialized as cubic perovskite structures and allowed to relax without constraints using plane augmented wave (PAW) pseudopotentials and the PW91 version of the generalized gradient approximation (GGA) without spin polarization employed through the VIENNA *ab initio* simulation package (VASP).[8] To provide a consistent k-space mesh, a k-point grid with target density 4000 k points/atom^{-1} and energy cutoff of 400 eV were utilized for final relaxation iterations after initial fast relaxation iterations were concluded with a reduced k mesh and energy cutoff.

B. Energy cluster expansion

Cluster expansion methods project first-principles derived and/or experimentally determined libraries of material

properties (e.g., energy, magnetic moment, dielectric tensor) onto a sum over an orthogonal basis set of topologically distinct clusters of sites representative of some crystallographic lattice. Reference 9 provides helpful demonstrations of a cluster basis set and Ref. 10 establishes the formal completeness of cluster expansion methodology. Here, we mention a few salient points. In its most primitive form, CE methods typically describe short-range pair and triplet correlations, and empirical formulations such as Heisenberg and Potts models have contributed considerably to understanding of collective properties and their correlations. Analogous to a Fourier transform in which a complex multivariate function is decomposed into a sum over a set of simple, orthogonal, weighted oscillatory functions, the CE decomposes the chosen material property into a sum over a set of topologically distinct, weighted crystallographic lattice site groupings, known as "clusters." In this context, the word cluster is not to be confused with a specific atomic/molecular configuration. In the example case of a structural energy CE constructed only from pair-wise clusters for a binary alloy with species A and B, the CE determines the optimal weighting coefficients (J_α below) for each unique lattice site pair (AA, AB, BB as nearest, next-nearest neighbor, etc.). Thus the system structural energy of the binary alloy with variable concentration A_xB_{1-x} and atomic configuration can then be constructed by summing over the average site occupation (multiplicity) of each unique pair multiplied by the pair's weight coefficient. In an expansion containing 1-, 2-, 3-... N-body terms, one commonly refers to the number of distinct sites comprising a particular cluster; e.g., "5-point clusters" contain five distinct lattice sites, which in turn have to be distinguished by their connectivity on the lattice.

The input data are frequently chosen from a training set of M specific physical structures (chemical composition, atomic arrangements) obtained from first principles calculations, and conditioned by experimental inputs and constraints. Clearly, the size of the input data set M and region of composition/configuration space it covers places a limit on the CE length and on its predictive power. A specific CE implementation requires choice of a method to define and minimize the error between the CE outputs and the inputs. The crossvalidation score, defined below, is a popular and statistically robust approach to determining the predictive power of a particularly selected set of topological clusters and the fit weights. One of the remarkable features of this approach is that all geometrical, atomic-position information due to atomic relaxations from the ideal lattice positions is efficiently absorbed into the cluster weights, thus permitting wide scale and rapid sampling of the physical composition and atomic configuration space.

A semianalytical equation describes the CE projection for the desired property using concentration and configuration space of a selected crystallographic topological structure as component variables. In the following, E is typically considered as the system cohesive energy or free energy, but as indicated above, the methodology can be applied to a host of other properties. While the summation in the following equation is formally complete (and infinite for an infinite lattice), the CE can be truncated to achieve a desired precision:[11]

$$E(\sigma) = \sum_{\alpha} m_\alpha J_\alpha \langle \varphi_\alpha(\vec{\sigma}) \rangle. \tag{1}$$

Here, m_α is the multiplicity of cluster α, J_α are the weighting/participation coefficients of cluster α, and $\langle \varphi_\alpha(\vec{\sigma}) \rangle$ are the lattice averages of the cluster functions defining distinct site groupings. One of the more subtle points of the CE scheme is determination of the most compact expansions that maintain precision while permitting physical interpretation of the coefficients. In general, this is accomplished by iteratively adding/deleting cluster terms and testing for significance.

As computational costs of first principles methods such as DFT limits model sizes below statistically interesting and thermodynamically significant levels, CE methods provide an attractive compromise between cost and accuracy. If a CE can be formed from DFT produced libraries with high precision, DFT-quality results can be replicated via statistical algorithms such as Monte Carlo sampling, permitting rapid searches of configuration and concentration space of realistically (nanometric) sized systems. Further, this formalism is readily extended to include vibrational and electronic free energies (see below), which can be important in determining favored chemical states and structural phases.

The CE approach used in the present work was built upon the alloy theoretical automated toolkit[12] (ATAT). Similar to our previous work,[3] CE cluster selection was optimized using a genetic algorithm. The primary fitness criterion in this scheme is chosen as the CE crossvalidation[11] (CV) score [see Eq. (2)]. Assuming a CE of structural energy, CV is defined as

$$\mathrm{CV} = \left\{ \frac{1}{N} \sum_{i=1}^{N} [E_i - E_i(\sigma)]^2 \right\}^{1/2}, \tag{2}$$

where E_i is the *ab initio* calculated energy of training structure i within the DFT calculated library of N system energies/configurations. The predicted CE energy $E_i(\sigma)$ of training structure i is found using the $N-1$ remaining structures to train the CE. Low-energy structures are sought after using an iterative approach where small structures, spanning concentration space, are calculated and a CE is optimized. Using the CE, new ground states are predicted and these are DFT calculated to obtain the structural energies after which a new CE is optimized. This process is repeated until no new ground states are predicted.

The addition of a vibration free energy CE to the structural energy CE provides a robust measure of the temperature dependence of the structural energy CE cluster weights. Nearest-neighbor interspecies stiffness versus length force equations (effective harmonic force constants) were fit from local perturbations of several of the structurally relaxed ground-state training structures. These training structures were selected across concentration space, and the resulting fit is confirmed to be well correlated to the included training structures' perturbative forces. Thus the stiffness versus length forces for arbitrary configurations of the material across concentration space are well represented within the set of thermally obtainable configuration states.

The resulting force equations were used to form k-space sampled dynamical matrices for each structure within the (zero temperature) CE training library. These dynamical matrices were used to determine each structure's vibrational spectrum within the harmonic approximation. From these harmonic-approximation spectra, vibrational entropies and

free energies were found by standard methods and added to the structural energy CE [see Eq. (3)]. The ensemble average of the vibrational free energies, at a given composition, is the property of interest for thermal properties. As the free energies are calculated as averages over phonon modes, errors tend to cancel out. A more complete description of this method and examples of previous applications can be found in Ref. 13.

$$J_\alpha(T) = J_\alpha + J_\alpha^{\text{vib}}(T). \quad (3)$$

Long-range electrostatic forces in ionic systems may in principle necessitate long-range force equation determination. A simple pair model of the electrostatic forces could be created and subtracted from the calculated forces, leaving the short-range forces to be represented using a simple spring model.[13] Similar treatment of the long-range electrostatic system energy is often necessary to construct a well converged structural energy CE. As this was not necessary for either LSCF or LSCR structural energy CE construction, explicit accounting of the long-range forces was deemed unnecessary in the present work.

C. Lattice Monte Carlo scheme

Once a high-precision energy CE is constructed (here, structural and vibrational energy), a lattice Monte Carlo (LMC) algorithm implemented within ATAT is employed to efficiently sample configuration space at fixed concentration of dopants and vacancies (Vacs), using the CE to determine the system energy. The LMC algorithm is thus deployed as a canonical ensemble model using the first-principles-derived energy CE as its fundamental input, providing structurally equilibrated free energy over a range of temperatures and concentrations. This approach is particularly well suited to determining optimized nanostructures of thermally equilibrated systems and their associated energies. Species swapping between crystallographically similar sites is unrestricted by activation energy barriers, in principle allowing all configurations to be sampled. Thus no explicit time scale exists within this model, as is found in CE-based kinetic Monte Carlo schemes,[14] and only the end points of an assumed diffusion path are considered. Additionally, since the present work is carried out in a bulk periodic supercell framework, no explicit surface structures, which may be important for nanoparticulate fuel cell material formulations, are represented. Furthermore, grain boundary structures, obviously important for bulk cation diffusion, are entirely absent from the model.

LMC equilibrated structures are analyzed primarily here using two-body atomic radial distribution functions and visual inspection of the large simulation volumes. Two-body atomic radial distribution functions $g_{ij}(r)$, such as inferred from extended x-ray absorption fine structure (EXAFS) and neutron diffraction, are useful in understanding structural data, average coordination sphere radii and site occupation number of component elements. As precise experimental atomic ordering data of nanostructured materials are still difficult to obtain, computation-based theoretical two-body radial structural analysis is an important tool to complement experimental determinations of the coordination and distribution of species.[15–17] Since distribution functions are inherently site-averaged quantities, they often give little insight into dopant/defect localized structure that can be clearly seen upon visualizing the thermally equilibrated model structures. Visualization approaches can reveal atomic clustering and domain formation that would otherwise be missed in standard sample averages.

As current CE methods project the energy onto clusters of topologically idealized lattice sites, atomic relaxations of LMC equilibrated structures cannot be recovered within the model framework. Therefore the theoretical distributions constructed here are necessarily discretized in terms of dimensionless coordination shells. In this description, each lattice location is at the focus of a sequence of regular coordination shells. A shell's type is described by its typical occupation, either anion or cation, and the percent species occupation of that shell. For instance, the Ru-Vac interaction is described as a focus Ru atom surrounded by a series of anion shells with vacancy occupancy at discrete, increasing radial distances, each with a determined percent (%) Vac occupation. In the case of, e.g., the Ru-Ru interaction, the first cation shell is synonymous with the second coordination sphere surrounding a Ru atom. Two-body distributions are completed by averaging the species occupation of neighbor sites of all equivalent sites, giving a description of local distributions and coordination numbers.

D. Electronic charge analysis

Bader topological density analysis[18] is used here for the determination of effective charge values of atoms within the extended solid. Bader analysis partitions the sample volume into distinct atoms by using zero-flux charge density surfaces to define atomic volumes. Advantages to this methodology lie in the consistent mathematical definition of atomic volumes, independent of basis sets or other computational factors, and in its successful use in interpreting molecular and solid chemical properties. Other definitions of ionic charge (such as the so-called R_{ws} Wigner-Seitz spherical volume integration scheme) typically rely on somewhat arbitrary assignments of atomic radii values assigned to the atomic nuclei, with each radius varied to match both the presumed oxidation state of the constituent atomic species and to fill space as well as possible. Such inconsistent accounting leads to regions of molecular space where charge density is either overcounted or simply not counted at all. Both R_{WS} and Bader schemes have their utility, however, in the present application, R_{WS} charge are generally far from expected formal values, and prove to be of little use in interpretation.

E. Transition states

Activation energies for point-to-point ionic hops are dependent upon both the local atomic configuration surrounding a hop-site as well as the nature of the transition path required to move between lattice points. A nudged elastic band (NEB) approach,[19,20] used to find minimum-energy transition paths between stable atomic lattice positions, can be used to determine diffusion pathways and their related activation energies. This methodology, as employed within DFT, performs a constrained relaxation on a set of intermediate image systems along the preassigned activation path. These image

systems are constrained by adding spring constants along the bands. Practically, the final image relaxation determines the diffusion path and the saddle point energy. There is no guarantee that the diffusion is dominated by a particular model process or path; thus intuition and experience play an important role. In particular, correlated processes such as simultaneous pair rotations or three-body exchanges can be overlooked. In the present work, only simple two-body jumps are treated, typically in the presence of an assisting vacancy, under the initial assumption that these processes are dominant.

F. Energy of substitution

The energy of substitution on a crystal sublattice (e.g., the A,A' or B,B′ sublattices in perovskites) can be calculated very easily with the present methodology. While this quantity does not directly enter in thermodynamic modeling, which assumes the existence of a given composition, it does give important physicochemical clues as to the ease/difficulty of forming the doped and alloyed structures. Previous theoretical studies have used similar energy methodologies, often to identify species favorable for doping into a host structure.[21,22] Using LSCF as an example, with chemical composition given in Eq. (4),

$$(La_x,Sr_{1-x})(Cr_y,Fe_{1-y})O_{3-\delta} \text{ with concentrations } x,\ y,\ \text{and } \delta. \tag{4}$$

The energy of substitution E_s on the B,B′ sublattice can be found as

$$E_s(x,y,\delta) = \lim_{y\to 0} \frac{[E_{\mathrm{LSCF}}(x,y-\Delta y,\delta) + E_{\mathrm{Cr}}(\Delta y)] - [E_{\mathrm{LSCF}}(x,y+\Delta y,\delta) + E_{\mathrm{Fe}}(\Delta y)]}{2\Delta y}. \tag{5}$$

Similar expressions apply to A, A' substitution and variable oxygen vacancy content. Using a CE to calculate bulk E_{LSCF} offers advantages over a straightforward DFT E_s calculation where a single atom is removed from or substituted within the periodic cell. First, Δy can be made very small in relation to y by increasing the system size. Additionally, LMC can be employed to simply reequilibrate the substituted system as it is not always clear what atom should be substituted to maintain a ground-state DFT configuration.

While the use of grand canonical LMC to determine explicit chemical potential versus composition relationships would be a more complete and elegant approach, the search through six-dimensional chemical potential space was considered potentially too costly for the present work. Further, while our CE representations were targeted for correct ground-state prediction within each concentration set of training structures, the grand canonical approach would have required high-quality prediction of relative formation energies between the concentration sets. For the present work, the outlined energy of substitution calculation via the canonical LMC allows the ability to perform the calculating with virtually no concentration change in our targeted structures, allowing us to capitalize on the work performed to ensure high-quality ground-state prediction.

III. RESULTS AND DISCUSSION

A. Cluster expansion model details

An LSCF (LSCR) CE was constructed from 192(182) structures, both stoichiometric and nonstoichiometric. Typical structures in the structural energy library range in size from 1 to 3 primitive cells. This feature highlights an advantage of the CE scheme: short-range interactions can be obtained immediately from small periodic samples, while long-range interactions are added via successively larger sample volumes. The CE for LSCF(LSCR) was optimized using a genetic algorithm that chose cluster sets from among 380(411) unique clusters, with maximum cluster sizes up to 7(7) lattice points. Of these possible clusters, 52(57) unique clusters were selected as an optimal set, containing up to 5(6) lattice point clusters. Both CEs fully spanned the full range of concentration space between A and A′ as well as B and B′. Oxygen vacancy (Vac) content was restricted to a maximum of 16.7% of the anion sublattice. This optimization resulted in a CV score of 11(13) meV per lattice site for LSCF (LSCR).

Correct structural energy ground states were accurately predicted for 33(32) of the 46(46) concentration sets calculated for LSCF(LSCR). Of the 13(14) concentration sets with predicted energies deviations from true DFT calculated ground state energies, the maximum deviation between the DFT-established low-energy structure and the CE-predicted low-energy structure was 9(22) meV with a median of 4(6) meV. Thus all structures erroneously predicted as low-energy states were low-energy structures themselves. Achievement of a low score with respect to the temperature regime (such as 25 meV at ∼300 K) is a fair evaluator of the predictive power of the CE, thus the CEs used here are deemed adequate. Convergence is considered good, especially as typical operational temperatures of SOFC components are often in excess of 1000 K. As outlined above, temperature dependence was also added to each CE through the inclusion of vibrational free energies and configurational entropy. A vibrational free energy CE was included with the structural energy CE of LSCF (LSCR), with a CV score of 0.9 (0.3) meV per lattice site.

A separate structural energy CE was constructed modeling the unsubstituted $(La_{1-x})(Cr_{1-y})O_{3-\delta}$ from 97 structures with a CV score of 4 meV. This CE was used to determine the energetics of A- and B-site cation vacancy formation, which then was used to find cation chemical potentials.

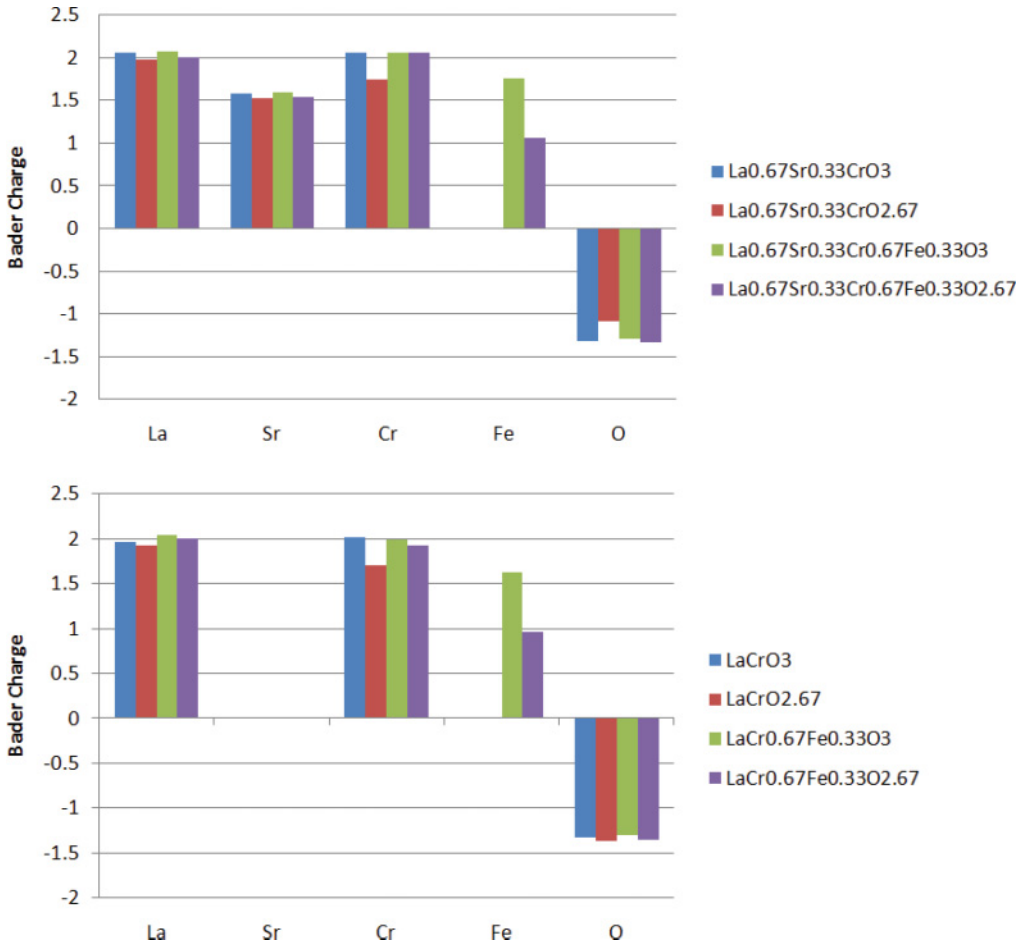

FIG. 1. (Color online) Bader analysis derived effective charges for LSCF structures with variable Cr, Fe, and O-Vac content. (a) Fixed $La_{0.67}Sr_{0.33}$ concentration, (b) Fixed $La_{1.0}$ concentration. Units are electron/atom, e; positive effective charge is electron deficient, i.e., cationic.

B. Electronic structure

1. *Effective charge*

Effective charges were calculated from the LSCF and LSCR training sets using Bader analysis as discussed above. Defining a *concentration set* as a group of sampled structures of given fixed composition, e.g., $La_{0.67}Sr_{0.33}Cr_{0.67}Fe_{0.33}O_{2.67}$, the lowest-energy specimen of each set was analyzed, with typical results shown in Figs. 1–2. Here, reduction processes were modeled by increasing vacancy concentration and oxidation was modeled by decreasing vacancy content. Any further chemical effects of actual reducing agents such as hydrogen and carbon monoxide were thus omitted.

The nominal ionic charges of La^{3+}, Sr^{2+}, Cr^{3+}, and Fe^{3+} are found to be overestimates according to Bader analysis, consistent with many previous theoretical studies. Nevertheless, the expected general trends are preserved, e.g., $Q_{La} > Q_{Sr}$ with a predicted difference of ∼0.5e. Significantly, Cr is predicted to be more ionic than either Fe or Ru, by ∼0.2–0.5e, depending upon the composition. Thus, for both LSCR and LSCF, Cr is more ionic than the B′ dopant (i.e., Fe and Ru). The addition of both Sr and the B′ dopants is seen to act to reduce the sensitivity of Cr atoms' charge to changes in the redox environment. Sr also enhances the reduction of B′ dopants as compared to their oxidized states. The effective Ru charge is notably more sensitive to oxidation and reduction than Fe in the presence of Sr dopants, having both a higher charge when there are no vacancies and a lower charge when vacancies are present.

2. *Density of states*

The partial density of states (PDOS) of two low-energy configurations of LSCF with composition $La_{0.67}Sr_{0.33}$ $Cr_{0.67}Fe_{0.33}$ and variable O-Vac content are shown in Fig. 3. In Fig. 3(a), the upper valence and conduction bands (UVB, CB) of Cr and Fe are seen to strongly overlap. This overlap, with a major peak at the Fermi energy (E_F), indicates strong contributions to the electronic conductivity. The bottom of the metal bands, around −7.5 eV, coincides with the bottom of the oxygen UVB, revealing the expected strong metal-oxygen covalent interactions. The main oxygen UVB terminates at about −2.5 eV, with weak but significant defect- and vacancy-related subbands occupying the region $\sim E_F$. The overlap of these "defect bands" with metal CB facilitates electronic transport across the neighboring cations. As expected, the La/Sr VB (found over −15 to −20 eV) play a negligible role in electronic transport; however, substructures seen to overlap with the

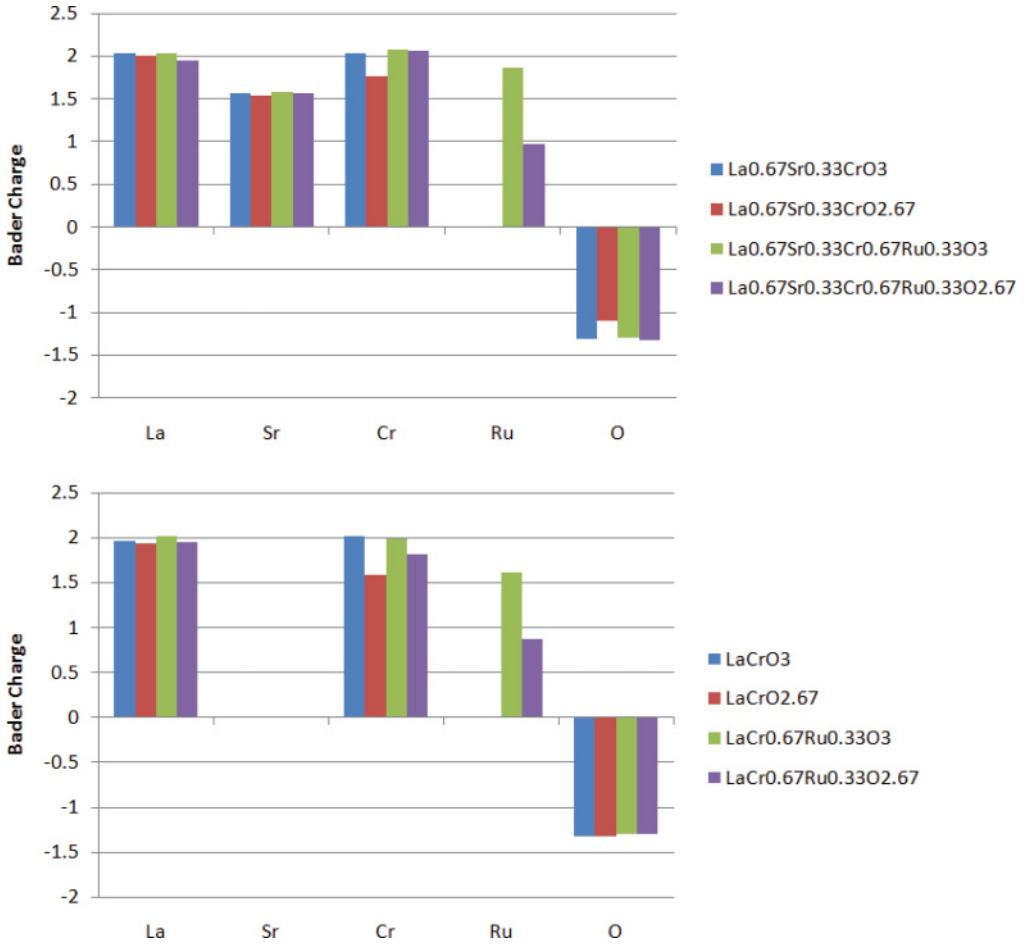

FIG. 2. (Color online) Bader analysis derived effective charges for LSCR structures with variable Cr, Ru and O-Vac content. (a) Fixed $La_{0.67}Sr_{0.33}$ concentration, (b) Fixed $La_{1.0}$ concentration.

oxygen LVB (lower valence band) indicate the di-cation-oxygen bonding interactions, which are particularly notable for La. In addition to the LVB splittings, weak La features are also observed in the oxygen UVB region, thus overlapping the lower portion of Cr/Fe bands, suggesting stronger electronic interaction of La compared to Sr. The vacancy concentration of the structure shown in Fig. 3(b) is higher by 11% as compared to the preceding O_3 configuration, thus both ionic charge transfer and covalent cation-anion interactions are expected to be noticeably reduced. Overlaying the two PDOS maps, we observe rather subtle and small band shifts. In general, all features described above for the vacancy-free composition are preserved, showing that the overall electronic structure is remarkably stable to (modeled) reduction.

The PDOS of two low energy configurations of LSCR with cation composition $La_{0.67}Sr_{0.33}$ $Cr_{0.67}Ru_{0.33}$ and variable O-Vac content are shown in Fig. 4. The structure shown in Fig. 4(a) shows features qualitatively similar to other $(A,A')(B,B')(O,Vac)_3$ systems, including the analogous LSCF structures just described. In detail, the Cr PDOS consists of an UVB coincident with the oxygen UVB representing covalent bonding interactions and extending down to ~8 eV below E_F. The Cr conduction band straddles E_F, with a major peak near the Fermi energy indicating strong contributions to electronic conductivity. The Ru UVB and CB are seen as a broad continuous structure with few strong peaks, extending to ~2.5 eV above E_F and coinciding with the top of the Cr CB. This cation overlap, assisted by the oxygen UVB and vacancy-derived oxygen states centered on E_F provides connectivity needed for good electronic conductivity. As seen previously, the La states play a small but noticeable role in the UVB region, with a major peak in the excited state region at ~2 eV above E_F. Sr states continue to play a negligible role in valence and low-lying excitation properties. The presence of vacancy defects in the structure shown in Fig. 4(b) reveals no significant differences, compared to the no-vacancy case, again attesting to the resilience of electronic structure in the redox environment.

C. Atomic ordering

Initial LMC equilibration calculations were carried out on periodic 30 × 30 × 30 supercells (~10.8 nm per side and 135 000 lattice points). It was determined that all extended ordering features found in this simulation volume could be observed in smaller cells. Therefore, all data reported here are from calculations on 20 × 20 × 20 cells (7.5 nm per side and 40 000 lattice points). Atomic ordering data were found by averaging quantities from six equilibrated structures, each initialized from a random distribution. All structures were

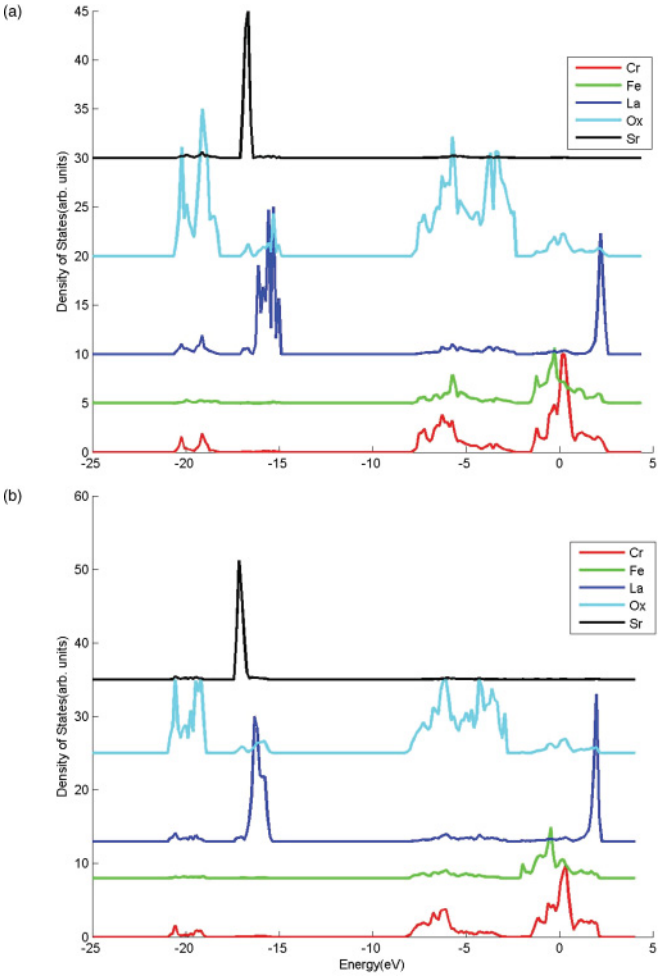

FIG. 3. (Color online) Partial densities of states for LSCF with fixed $La_{0.67}Sr_{0.33}$ $Cr_{0.67}Fe_{0.33}$ composition and varying O-Vac content. (a) O_3 and (b) $O_{2.67}$.

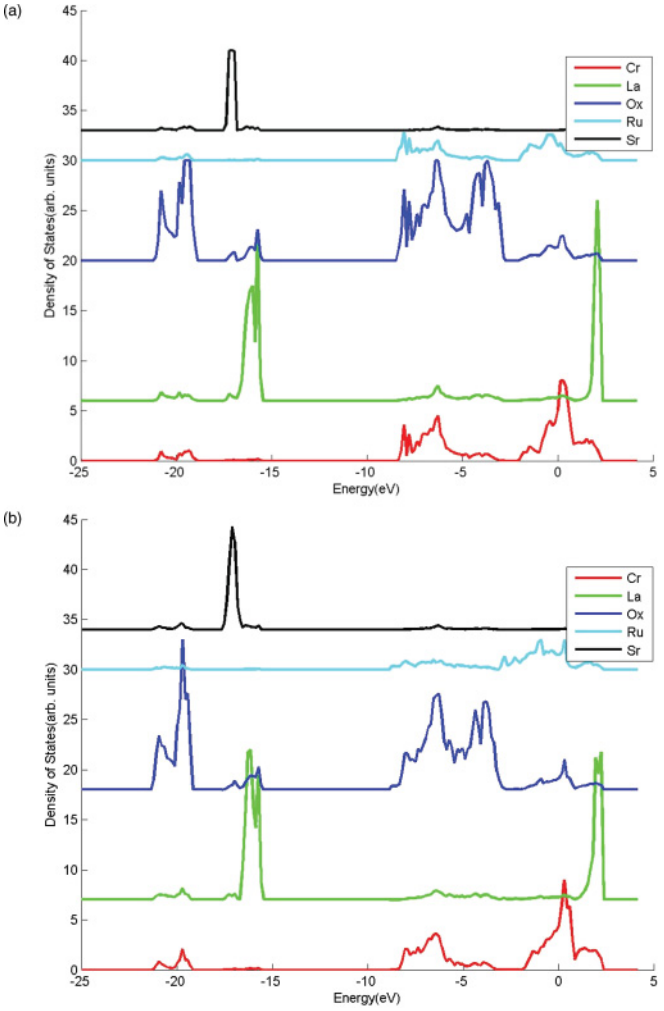

FIG. 4. (Color online) Partial densities of states for LSCR with composition $La_{0.67}Sr_{0.33}Cr_{0.67}Ru_{0.33}$ and variable O-Vac content. (a) O_3, (b) $O_{2.67}$.

equilibrated at 1000 K and only atomic exchanges between neighboring cells were permitted so as to reflect equilibration processes in real materials where atoms are limited to near-range hops.

As oxygen anion diffusion is much faster than the metal cation diffusion, it is reasonable as a first step to solely allow anion equilibration within fixed randomly distributed cations. This method helps isolate oxygen vacancy ordering for analysis and perhaps adequately models an "as-synthesized" system. Similarly, as Ru diffusion is of great interest within this study, it is useful to isolate B-site ordering by equilibrating both B sites and anion sites while leaving A sites fixed and randomly distributed. This A-site restriction may seem a contrivance for modeling purposes as Cr diffusion in lanthanum perovskites is known to be orders of magnitude slower than that of La or Sr.[23] Yet, Ru nanoparticles are seen to rapidly precipitate within 15 minutes onto surfaces of nanoparticles of LSCR upon annealing under reducing conditions.[4] Calculations of rigorous relative diffusion rates of the various constituent cations are outside the scope of this theoretical study; NEB estimates of selected barrier heights and related activation energies are discussed below. Lastly, a third set of calculations was performed where all atoms were allowed to simultaneously thermally equilibrate.

Within this study, all ordering data are presented here as "percent excess coordination:"

$$\gamma_{\text{excess}} = \frac{C_{\text{equilibrated}} - C_{\text{random}}}{C_{\text{max}}} \times 100. \tag{6}$$

Here, $C_{\text{equilibrated}}$ is the coordination number of a specific species within a coordination shell with maximum coordination C_{max} and C_{random} is the expected coordination of the randomly distributed system with equal concentration. This presentation of the data aids in discerning attractive and repulsive ordering tendencies as well as cleanly displaying ordering differences between structures with varying concentrations. If a coordination shell has a 0% excess coordination, that shell's percent coordination is equal numerically to the expected percent coordination of a randomly distributed system with the same concentration. Explicitly, as the third to seventh Ru-Vac interactions (see below) have essentially 0% coordination, the equilibrated percent coordination of the LSCR system with $\delta = 0.1$ is ~3.33%.

Increased reduction of the material is modeled by increasing oxygen vacancy content. Periodic cell DFT distributions enforce charge neutrality within the system cell. Therefore removing oxygen atoms induces the (excess) electrons previously associated with the oxygen anions to redistribute over the remaining atoms in the cell, modeling reduced electronic interactions. Decreasing vacancy content, similarly, models an increasingly oxidized environment; however, we do not considered interstitial oxygen and related hypercoordination, as this is incompatible with the present lattice model.

The same simulations were performed for each of the three levels of equilibration (i.e., anion-only, fixed A-site, and unrestricted); however, only a selected portion of the resultant data is displayed here. This study resulted in more ordering data than can conveniently be presented while maintaining focus on the main thrust of discussion. Some of the omitted coordination data may be of some use to others, however, and are included in Supplemental Material.[24]

1. *Redox-dependent equilibration*

Different redox environments were modeled by varying the oxygen content of otherwise similar materials. The depletion/addition of oxygen atoms induces a reductive/oxidative environment by changing the number of electrons associated with the remaining atoms. Referring to the chemical formulas for LSCF and LSCR in Sec. I, Sr content is 20% of the A site ($x = 0.2$), Fe/Ru account for 18% of the B site ($y = 0.18$), and oxygen levels were set ($0 \leqslant \delta \leqslant 0.2$) to model several redox environments where lower δ models more oxidized systems and higher δ models more reduced systems. Interaction data are presented in Figs. 5–9. All shells represent sequentially longer range interaction data within a 1-nm radius of the focus atoms. For purposes of brevity, solely data from the "unrestricted" model equilibrations are presented as figures and deviations of these data from the "anion-only" and "fixed A-site" models are discussed.

Figure 5 shows Vac-Vac ordering data for both LSCF and LSCR. Vacancies in LSCF tend to strongly cluster in sets of three, with excess up to 20% in the first anion coordination shell; clusters also show a characteristic long-range ordering at the eighth anion shell for more highly reduced ($\delta = 0.1$ and $\delta = 0.2$) systems. Vacancy ordering for LSCF changes only slightly from "anion-only" to "fixed A-site" equilibration results, showing that to first-order, vacancies do not discriminate among cations. Again, it bears emphasis that though, for instance, shells 9–13 have ~0% excess coordination, these coordination shells have vacancy concentration equal to that expected for a randomly distributed structure, not absolute 0% coordination.

LSCR similarly prefers clustering of vacancies but the clusters are neither as tightly packed nor show such pronounced long-range ordering. LSCR first anion Vac shell clustering increases significantly upon reduction, with clear peaks at 2nd (15%) and 4th–5th shells. Comparing Vac clustering of the "unrestricted" equilibration model [see Fig. 5(b)] with the "anion-only" and "fixed A-site" data shows an enhancement of ordering (both attractive and repulsive) of all the shells occurring upon Ru equilibration. This indicates

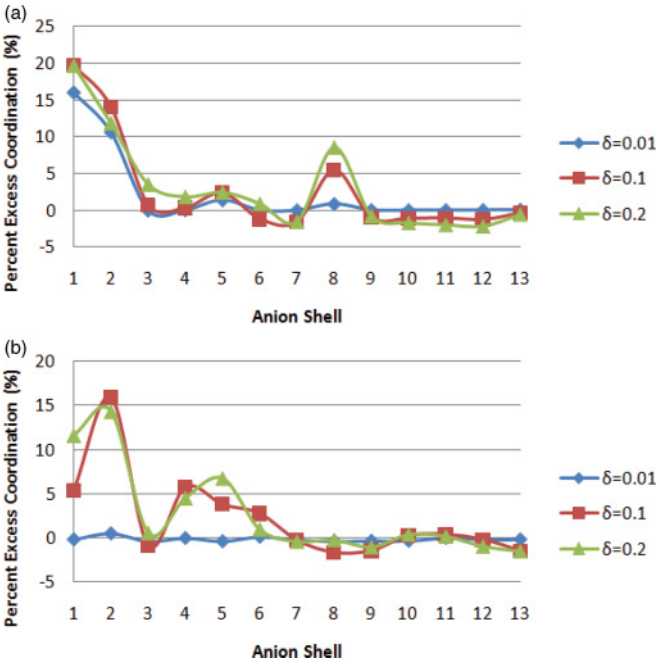

FIG. 5. (Color online) Vac-Vac interactions sequentially ordered by coordination shell for (a) LSCF and (b) LSCR with anion equilibration. δ refers to the value in the chemical formulas for LSCF and LSCR found within Sec. I. Vertical axis represents deviation from the expected random distribution value as a percentage of each shell's coordination number.

a discrimination (we shall see that it is a preference) for Ru among various cation types present.

Sr-Vac interactions within the "unrestricted" model are shown in Fig. 6. Both LSCF [see Fig. 6(a)] and LSCR [see

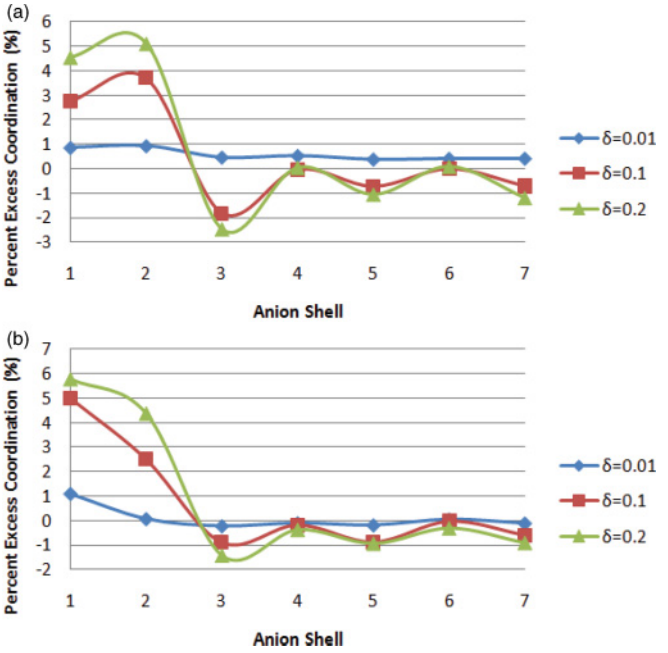

FIG. 6. (Color online) Sr-Vac interactions sequentially ordered by coordination shell for (a) LSCF and (b) LSCR with unrestricted equilibration.

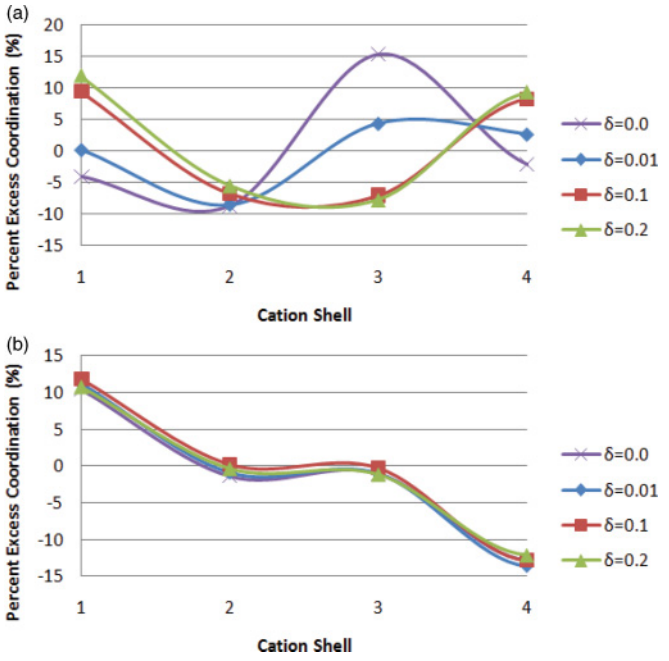

FIG. 7. (Color online) Sr-Sr interactions sequentially ordered by coordination shell for (a) LSCF and (b) LSCR with unrestricted equilibration.

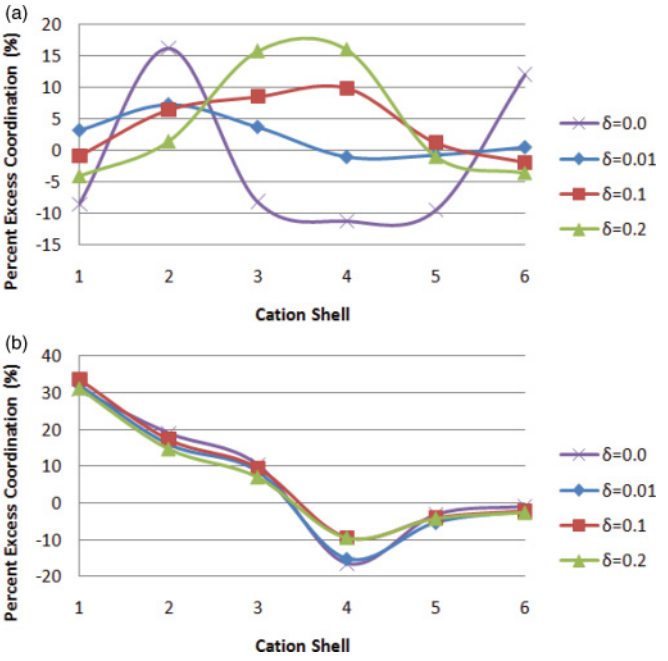

FIG. 9. (Color online) B′-B′ interactions sequentially ordered by coordination shell for (a) LSCF and (b) LSCR with unrestricted equilibration.

Fig. 6(b)] materials show low (5–6% excess attraction in shells 1, 2 and 1–2% excess repulsion in shells 3, 5) but definite short-range ordering in the more reduced systems. The most oxidized structures ($\delta = 0.01$) show an almost complete lack of interaction between the Sr and Vac species. Comparison with the "as-synthesized" and "fixed A-site" models reveals that though Sr-Vac interactions for oxidized structures are virtually the same across models, the ordering in the more reduced structures only occurs upon Sr equilibration for both LSCF and LSCR; there are virtually zero interactions between species otherwise with only hints of the ordering found upon Sr equilibration. The generally small Sr-Vac interaction may be surprising, since Sr^{+2} and Vac are nominally oppositely charged and could be expected to form charge compensating complexes. The relatively small Bader charge differences between La and Sr noted previously may help to rationalize the predicted rather weak interactions.

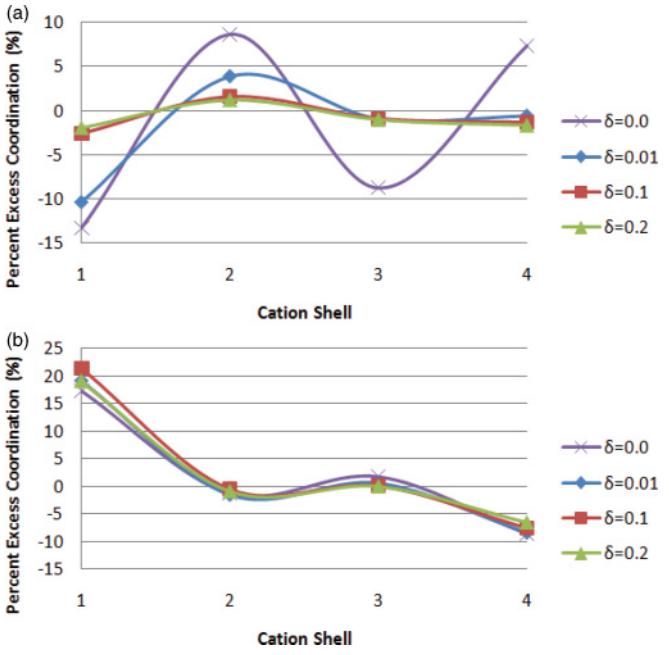

FIG. 8. (Color online) B′-Sr interactions sequentially ordered by coordination shell for (a) LSCF and (b) LSCR, both with unrestricted equilibration.

Sr-Sr interactions, only calculated within the "unrestricted" model, show distinctive ordering (see Fig. 7). Visualization of the reduced LSCF structures (δ ~0.1–0.2) shows first cation shell Sr-Sr chains and sheets, usually three to six Sr atoms long upon oxidation (δ ~0.0 and 0.01), the ordering distances increase in range with Sr occupation filling the available volume more broadly. As might be supposed from the ordering seen in Fig. 7(b), Sr in LSCR form small clusters of, often, two to eight Sr atoms (on neighboring cation sites, of course; antisite ordering is not considered). From the ordering of Sr-Sr in LSCR, one can also see that these clusters tend to strongly repulse each other, causing them to fill the volume in a fairly even manner. The larger clusters could be said to be nucleating a strontium oxide nanophase dispersed in the bulk.

Figure 8 shows the Fe-Sr and Ru-Sr interactions. While Fe-Sr interactions [see Fig. 8(a)] exhibit strong ordering when oxidation levels are high, (repulsion in 1st and 3rd shells, attraction in 2nd) reduction serves to practically nullify the Fe-Sr interaction. Note that in LSCR the Ru-Sr ordering [see Fig. 8(b)], as with the Sr-Sr interactions, is largely insensitive to the redox environment. Comparing data from the "unrestricted" model [see Fig. 8(b)] with those derived from the fixed A-site, there is strong similitude between the two

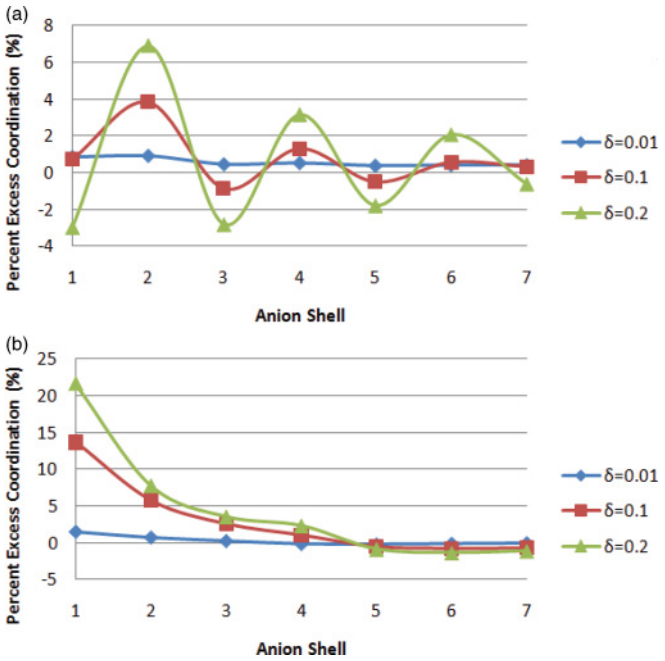

FIG. 10. (Color online) B′-Vac interactions sequentially ordered by coordination shell for (a) LSCF and (b) LSCR with both anion and B-site equilibration.

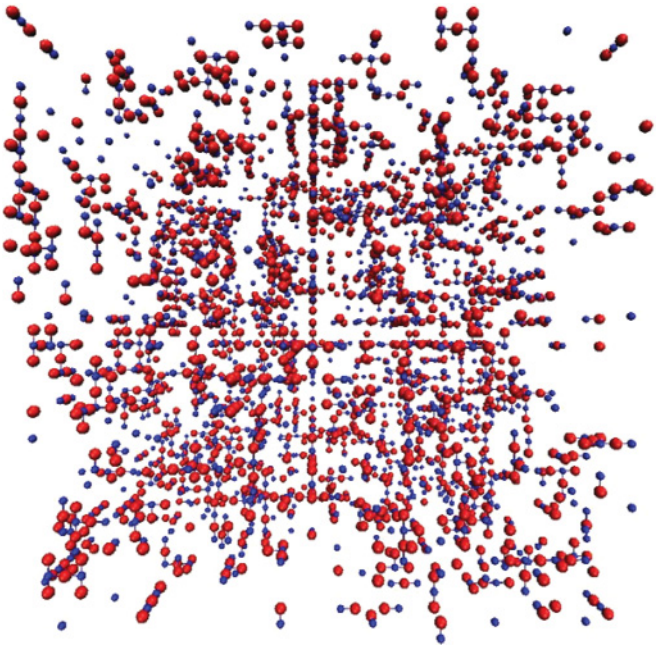

FIG. 11. (Color online) Random Ru and equilibrated oxygen vacancy positions of a 20 × 20 × 20 cell in the "anion-only" equilibration model at 1000 K. Small and blue: Ru; large and red: oxygen vacancy.

models. Quantitatively, the peak percent excess coordination of the first cation Ru-Sr shell of LSCR is reduced to ∼6% and the 4th cation Sr shell is diminished to about −1% when the A site is not allowed to equilibrate. When the A-site cations are not allowed to equilibrate, ordering of the most oxidized LSCF structure ($\delta = 0.0$) is almost exactly the same as the ordering of the $\delta = 0.01$ structure.

B′-B′ interactions (Fe-Fe and Ru-Ru) exhibit distinctive ordering patterns (see Fig. 9). Similar to B′-Sr, Fe-Fe interactions [see Fig. 9(a)] show long-range ordering (with alternating excesses extending at least out to the 6th shell) and Ru-Ru interactions [see Fig. 9(b)] show extremely strong short-range ordering (30% attractive excess in the 1st shell). Also, similar to the B′-Sr interactions, the most oxidized LSCF structure ($\delta = 0.0$) is almost exactly the same as the ordering of the $\delta = 0.01$ structure when the A-site cations are fixed. Unlike the B′-Sr interactions, the strength of the attractive and repulsive ordering is almost entirely unchanged upon A-site equilibration.

B′-Vac interactions (see Fig. 10) reveal that oxidized structures are very insensitive to the B′ atom locations; i.e., the correlations seem to be purely random. Upon increasing levels of reduction, however, oscillatory LSCF structures [see Fig. 10(a)] have increasing long-range Fe-Vac ordering (e.g., 7% excess attraction at the 2nd shell) while LSCR structures [see Fig. 10(b)] exhibit increasing short-range Ru-Vac interactions (up to 21% excess at the 1st shell). There are virtually no differences found in ordering between the "unrestricted" and fixed A-site models. Comparing with the "anion-only" model, Fe-Vac ordering is still oscillatory but only extends to the fifth anion Vac shell and decreases in amplitude. Similarly, Ru-Vac interactions are much shorter in the anion-only model, involving only the first anion Vac shell, and reduced in amplitude. This clearly indicates a strong Ru-Vac correlated ordering tendency, which is hindered in as-synthesized materials, but activated under normal thermal operating conditions.

The experimentally observed rapidity of Ru diffusion onto the surface of reduced LSCR nanoparticles suggests that the mechanism of rapid diffusion will be found in the as-synthesized material, not due to cation clustering after a significant break-in period. Visualizing the anion-only $\delta = 0.2$ LSCR structure, one can easily see that oxygen vacancies prefer to nest between two nearest-neighbor Ru atoms (see Fig. 11). A prominent feature of Ru-Vac ordering is the presence of 2D clusters, not linear chains, of Ru-Vac associates such as those shown in Fig. 12. It is expected that a swap between nearest-neighbor Ru-Cr lattice positions would be aided by such 2D associates as additional anion vacancies provide an increasingly clear diffusion path. Though not all associates contain a neighboring Cr atom available to swap, associates like those found in Fig. 12 are not rare within any applied model (Table I). The number of multivacancy Ru-Vac associates is large compared to "anion-only" LSCF; the number of Fe-Vac associates like those found in Fig. 12 is

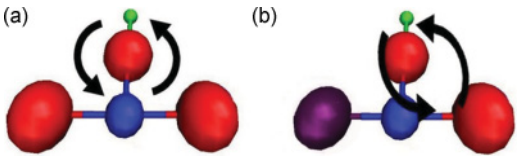

FIG. 12. (Color online) 2D Ru-Vac associates sampled from structure seen in Fig. 11 with (a) three and (b) two nearest-neighbor oxygen vacancies. Arrows denote a proposed coordinated diffusion mechanism aiding the swap of Ru and Cr atoms. Tiny/green: Cr, Small/blue: Ru, Medium/purple: O, Large/red: oxygen vacancy.

TABLE I. Typical content of Ru first anion Vac shell.

Number of vacancies	Anion-only:% of total Ru	Fixed A-site:% of total Ru	Unrestricted A-site:% of total Ru
0	24.7	5.9	7.7
1	43.4	56.4	53.4
2	9.8	2.8	4.2
3	21.8	31.9	29.8
4	0.4	3.1	4.9

only ∼0.3%. As Ru-Ru interactions have the highest percent excess coordination found for any interaction type in either material regardless of A-site equilibration or redox levels, both the driving force as well as the means to combine isolated Ru-Vac associates into large Ru-rich and O-poor regions is available. The "unrestricted" LSCR model presented here shows significant Ru-Sr interaction strength but it is not clear how quickly Sr atoms can cluster or what effect that would have on Ru diffusion.

These interaction results present a stark contrast between atomic ordering of LSCF and LSCR in different redox environments. Whereas interactions directly involving Fe in reduced LSCF demonstrate long-range ordering, thereby decreasing Fe's expected mobility, reduced LSCR Ru interactions are strictly short-range. While there are virtually no 2D Fe-Vac associates in LSCF, there are substantial numbers of 2D Ru-Vac associates to open up Ru diffusion pathways. From these results alone, it may be expected that Ru atoms have an enhanced diffusion rate over Fe atoms.

D. Transition state

Motivated by the unusually high anion vacancy clustering around Ru cations found in the atomic ordering results of reduced LSCR, initial transition state calculations were conducted in the hopes of clues to the mechanism of fast Ru diffusion. Activation energies of diffusion for the 2D Ru-Vac associations were determined using a NEB methodology as implemented within the VASP code. Two periodic cells, each with 135 lattice points, were constructed. The first cell contains the activation path with the 2D Ru-Vac associate seen in Fig. 12(a) and the second with the 2D Ru-Vac associate seen in Fig. 12(b). Though no atoms within the cell were fixed, the perovskite lattice for both structures was insignificantly perturbed, easily incorporating the unusual high vacancy associates. This stability corroborates the mechanical stability of the perovskite structure even with high-density vacancy clusters present. Surprisingly, both the associates shown in Fig. 12 followed a diffusion path similar to that seen in 12(b), with the Ru atom sliding first into the neighboring oxygen vacancy before swinging into the position previously vacated by the Cr atom. By visual inspection, the three-vacancy associate did not utilize the extra vacancy in the lowest-energy diffusion pathway. The energy of activation (E_A) for each, however, differed greatly. NEB calculations resulted in $E_A = 13.4$ eV for two-vacancy 2D Ru-Vac associates and $E_A = 7.4$ eV for three-vacancy 2D Ru-Vac associates. These results compare well to previous atomistic calculations[25,26] of direct B site migration via cation vacancies in $LaGaO_3$. Theoretical results, however, deviate significantly with experimental findings, showing bulk Cr diffusion E_A to be 2.2 eV and grain diffusion E_A to be 2.8 eV.

This disparity between experimental and theoretical expectations of E_A for B-site diffusion has been noted elsewhere[27] and suggests the presence of a somewhat exotic diffusion mechanism. Schulz *et al.* proposed a cooperative diffusion mechanism involving two anion vacancies, a B-site vacancy, and an A-site vacancy. The cooperative diffusion mechanism decreases B-site E_A by eliminating the need for the B-site cation to cross near the A-site cation, and its large Coulombic repulsion, upon diffusion. The proposed mechanism was corroborated with theoretical atomic simulations.[28] Transition state results here reported suggest that 2D Ru-Vac associates, especially the three-vacancy associates abundant in reduced LSCR, can greatly reduce the energetic cost of swapping between two occupied lattice positions. In essence, 2D Ru-Vac associates energetically mimic cation vacancies for purposes of cation diffusion.

These results suggests a possible, though speculative, fast Ru diffusion mechanism in reduced LSCR. Where cation mobility is typically limited by both high activation energies and dilute amounts of cation vacancies, 2D Ru-Vac associates provide a means for cation swapping, comparable in energetic cost to hops via cation vacancies. If, as Bader analysis suggests, Ru atoms have notably lower positive charge than Cr when reduced, the electric potential could act under the same basic principle as a centrifuge, favoring the diffusion of the less positive Ru atoms away from the electrolyte and onto the surface of the materials and the more positive Cr atoms toward the electrolyte. Cation diffusion would proceed by a series of swaps mediated by the abundant high anion vacancy clusters. Similarly, as Sr has lower positive charge than La atoms, the anode surface of reduced, operationally aged LSCR is expected to have increased Sr content, in addition to Ru precipitate.

E. Substitutional energy

Substitutional energy was calculated as previously outlined. To minimize errors, five substitutional energy calculations were performed for each structure at 0 K on 25 × 25 × 25 supercells (78 125 lattice points) and results were averaged across the five separate structures. Each substitutional energy calculation was performed on a different randomly generated yet equal concentration structure. Approximately 80 of the variational species [Δy in the example given in Eq. (5)] for each of the five separate calculations were substituted using random selection to meet the Δy requirement of

TABLE II. Energy of substitution of lanthanum chromates. For example, the energy of substitution for type Fe/Cr is given as the energy change as one Fe is substituted for Cr in the extended crystal lattice. RMSE is the root mean square error over sampled configurations; see text.

Structure	Concentration	Substitution	Energy per substitution (eV)	RMSE (eV)
LCO3	$LaCrO_3$	Vac/La	5.36	0.02
LCO3	$LaCrO_3$	Vac/Cr	8.92	0.01
LSCF	$LaCrO_3$	Fe/Cr	3.12	0.00
LSCF	$(La_{0.8},Sr_{0.2})CrO_{2.9}$	Fe/Cr	−1.74	0.38
LSCF	$La(Cr_{0.82},Fe_{0.18})O_3$	Fe/Cr	2.94	0.05
LSCF	$(La_{0.8},Sr_{0.2})(Cr_{0.82},Fe_{0.18})O_{2.9}$	Fe/Cr	2.23	0.89
LSCR	$LaCrO_3$	Ru/Cr	3.15	0.01
LSCR	$(La_{0.8},Sr_{0.2})CrO_{2.9}$	Ru/Cr	−0.14	0.09
LSCR	$La(Cr_{0.82},Ru_{0.18})O_3$	Ru/Cr	2.60	0.39
LSCR	$(La_{0.8},Sr_{0.2})(Cr_{0.82},Ru_{0.18})O_{2.9}$	Ru/Cr	1.81	0.57

Eq. (5). Sr and oxygen vacancy concentrations were kept fixed at a 2:1 ratio in an attempt to maintain effective-charge neutrality.

The energies of isolated atoms [e.g., $E_{Cr}(\Delta y)$ of Eq. (5)] were found within the DFT framework by calculating a single atom in a cube with side length 25 Å using a spin-polarized exchange-correlation approximation. All training structures used to construct the CEs were calculated without spin polarization, thus the spin-polarized GGA correction for atomic Ru, Cr, and Fe as found within the VASP manual[29] was applied to make an appropriate comparison with the bulk energies.

To determine the substitutional energy of systems close to their as-synthesized state, anion equilibration only was initially allowed. This procedure led large root-mean-square errors (RMSE) across the five separate calculations, presumably due to unfavorable energetics of the randomly distributed A-site cations relative to the B-site cations. To resolve this issue, full anion equilibration was completed followed by a single B-site cation equilibration pass with results reported in Table II. Results suggest that the presence of Sr cations facilitates doping of the B-site cation in both LSCF and LSCR structures. As B-site dopant concentrations increase, the energy favorability of the substitution decreases. The energy neutral balance point for Ru/Cr substitution in LSCR is close to 0% Ru dopant levels, suggesting Cr may always be favored within the crystalline structure for all levels of Sr dopants. The cost to generate a B-site vacancy, however, seems quite large in the undoped, neutral $LaCrO_3$ structure.

IV. CONCLUSIONS

A temperature-dependent cluster expansion of doubly substituted perovskite oxides with formula $(La_x,Sr_{1-x})(Fe_y,Cr_{1-y})O_{3-\delta}$ and $(La_x,Sr_{1-x})(Ru_y,Cr_{1-y})O_{3-\delta}$ was constructed from a library of structures calculated via first principles. Good precision in predicted structural energy was found over the entire composition range studied $(0 < x < 1, 0 < y < 1, 0 < \delta < 0.5)$ with typical crossvalidation scores of ∼11(13) meV/lattice site for LSCF (LSCR). Lattice Monte Carlo sampling based upon the cluster expansions at finite T was used to determine A′, B′, and Vac (oxygen vacancy) defect ordering as the simulated redox environment was varied. Reduction/oxidation was modeled simply by controlling oxygen content of the simulation volumes. Atomic ordering structural findings (outlined below) motivated further calculations to explore electronic structure, B-site transition states, and the energies of substitution.

Bader analysis of the electronic charge densities of ground-state structures shows that, upon system reduction, the B-site dopants (Fe and Ru) are the primary electron acceptors. In the absence of such dopants, in reducing conditions, the Cr atom acts as the primary electron acceptor. Further, comparing similarly composed LSCR and LSCF structures, the charge associated with Ru dopant atoms is computed to be more sensitive to redox changes than Fe. Partial densities of states were obtained by projecting electronic wave function character onto the energy spectrum. Both LSCF and LSCR show well defined metal valence and conduction bands that are remarkably stable against the limited composition range studied here. Quantitative shifts and broadening of metal features were observable, including those around E_F, which are critical to electronic conduction processes. The broad overlap of metal and oxygen *sp* valence bands attests to the strong contributions of metal-ligand covalency to structural stability and labile charge flow in the doped oxide perovskites.

Energies of cation substitution and vacancy defect formation were calculated using a CE-based LMC approach, and appear to be consistent with literature data for similar systems; lattice relaxation clearly plays a major role in quantitative values of such energetics. It is therefore remarkable that these structural data, which are represented only implicitly in the cluster expansions, are so adequately reproduced and thus usable in large-scale MC simulations. Certain unsuspected correlations in energetics versus composition can be detected in the data, although no general phase-field survey was made. For example, the Ru/Cr substitution energy of 3.15 eV in $LaCrO_3$ is in stark contrast to the value of −0.14 eV in the charge equilibrated $(La_{0.8}Sr_{0.2})CrO_{2.9}$, suggesting that the solubility and even kinetic factors relating to diffusion are a strong function of composition with significant opportunities yet to be explored.

The principal structural findings are that (1) Ru has strong, short-range ordering with oxygen vacancies and neighboring Ru and there exists strong affinity for Sr to equilibrate near Ru atoms. Interactions are relatively insensitive to redox

conditions. (2) 2D Ru-Vac associates provide plentiful wide diffusion paths, possibly helping enable fast Ru diffusion. (3) Fe has moderate strength, long-range ordering with oxygen vacancies and Fe under reducing conditions. Oxidation diminishes the strength of Fe-Vac interactions. Moderate strength Fe-Sr interactions fade upon reduction.

The B-site transition findings are that (1) nearest-neighbor anion vacancy clusters around Ru atoms (2D Ru-Vac associates), as seen in reduced LSCR systems, diminish the activation energy required for Ru-Cr swaps. (2) NEB calculations show that activation energies of anion vacancy mediated B-site swaps are comparable in size to B-site cation hops onto cation vacancies. (3) The abundance of mediating 3-vacancy 2D Ru-Vac associate clusters of three oxygen vacancies could provide the means for fast Ru diffusion in reduced LSCR systems.

Static atomic ordering implies a novel mechanism for dynamic diffusion processes via 2D anion vacancy associates. Further exploration of cooperative diffusion of Ru and Sr atoms via other theoretical methodologies, such as molecular dynamics, is warranted. Additionally, experimental studies can be conducted to determine if higher concentrations of Sr are found on anion surfaces. Application of combined theoretical procedures which include CE methodologies to additional multicomponent mixed ionic/electronic conductors would be helpful in identifying globally important effects, as distinct to the chemistry and lattice structure of the LSCF/LSCR systems reported here.

ACKNOWLEDGMENTS

Work supported by the US Department of Energy, Basic Energy Sciences, under Award Number DE-FG02-05ER46255, by the US National Science Foundation under Grant DMR-0953378 and by Teragrid Resources provided by NCSA under Grant No. DMR050013N.

*don-ellis@northwestern.edu

[1] A. B. Stambouli and E. Traversa, Renew Sust. Energ Rev. **6**, 433 (2002).

[2] [http://www.fossil.energy.gov/programs/powersystems/fuelcells/].

[3] P. Dalach, D. E. Ellis, and A. van de Walle, Phys. Rev. B **82**, 144117 (2010).

[4] Y. Wang, B. D. Madsen, W. Kobsiriphat, S. A. Barnett, and L. D. Marks, Microsc Microanal. **13**, 100 (2007).

[5] T. Ramos and A. Atkinson, Solid State Ionics **170**, 275 (2004).

[6] B. D. Madsen, W. Kobsiriphat, Y. Wang, L. D. Marks, and S. A. Barnett, J. Power Sources **166**, 64 (2007).

[7] W. Kobsiriphat, B. D. Madsen, Y. Wang, L. D. Marks, and S. A. Barnett, Solid State Ionics **180**, 257 (2009).

[8] G. Kresse and J. Hafner, Phys. Rev. B **49**, 14251 (1994); **47**, 558 (1993); G. Kresse and J. Furthmuller, Comp. Mater. Sci. **6**, 15 (1996); Phys. Rev. B **54**, 11169 (1996).

[9] A. Van der Ven, M. K. Aydinol, G. Ceder, G. Kresse, and J. Hafner, Phys. Rev. B **58**, 2975 (1998).

[10] J. M. Sanchez, F. Ducastelle, and D. Gratias, Physica A **128**, 334 (1984).

[11] A. van de Walle and G. Ceder, J. Phase Equilib. **23**, 348 (2002).

[12] A. van de Walle, M. Asta, and G. Ceder, Calphad. **26**, 539 (2002).

[13] A. van de Walle and G. Ceder, Rev. Mod. Phys. **74**, 11 (2002).

[14] A. Van der Ven, J. C. Thomas, Q. C. Xu, B. Swoboda, and D. Morgan, Phys. Rev. B **78**, 104306 (2008).

[15] G. E. Rush, A. V. Chadwick, I. Kosacki, and H. U. Anderson, J. Phys. Chem. B **104**, 9597 (2000).

[16] P. Ghigna, M. Di Muri, and G. Spinolo, J. Appl. Crystallogr. **34**, 325 (2001).

[17] E. Curis and S. Benazeth, J. Synchrotron. Radiat. **12**, 361 (2005).

[18] R. F. W. Bader, *Atoms in Molecules: A Quantum Theory, International Series of Monographs on Chemistry* (Clarendon, Oxford, 1990).

[19] H. Jonsson, G. Mills, and K. W. Jacobsen, *Nudged Elastic Band Method for Finding Minimum Energy Paths of Transitions, in Classical and Quantum Dynamics in Condensed Phase Simulations* (World Scientific, Singapore, 1998).

[20] D. Sheppard, R. Terrell, and G. Henkelman, J. Chem. Phys. **128**, 134106 (2008).

[21] M. T. Buscaglia, V. Buscaglia, M. Viviani, and P. Nanni, J. Am. Ceram. Soc. **84**, 376 (2001).

[22] M. Saiful Islam, J. Mater Chem. **10**, 1027 (2000).

[23] T. Kawada, T. Horita, N. Sakai, H. Yokokawa, and M. Dokiya, Solid State Ionics **79**, 201 (1995); T. Akashi, M. Nanko, T. Maruyama, Y. Shiraishi, and J. Tanabe, Proceedings of the Fifth International Symposium on Solid Oxide Fuel Cells (Sofc-V) **97**, 1263 (1997); T. Horita, M. Ishikawa, K. Yamaji, N. Sakai, H. Yokokawa, and M. Dokiya, Solid State Ionics **108**, 383 (1998); **124**, 301 (1999); N. Sakai, K. Yamaji, T. Horita, H. Negishi, and H. Yokokawa, *ibid.* **135**, 469 (2000).

[24] See Supplemental Material at http://link.aps.org/supplemental/10.1103/PhysRevB.85.014108. The supplementary materials provide additional atomic ordering data which was not easily represented within the scope of the manuscript. Data are represented according to the extent of atomic equilibration (anion-only, Fixed A-site, and Unrestricted) in its raw, spreadsheet format.

[25] M. S. Khan, M. S. Islam, and D. R. Bates, J. Phys. Chem. B **102**, 3099 (1998).

[26] R. A. De Souza and J. Maier, Phys. Chem. Chem. Phys **5**, 740 (2003).

[27] O. Schulz, M. Martin, C. Argirusis, and G. Borchardt, Phys. Chem. Chem Phys **5**, 2308 (2003).

[28] M. Kilo, M. A. Taylor, C. Argirusis, G. Borchardt, R. A. Jackson, O. Schulz, M. Martin, and M. Weller, Solid State Ionics **175**, 823 (2004).

[29] [http://faculty.mint.ua.edu/~ph585/vasp/node209.html].